Measuring Ti(III)−Carotenoid Radical Interspin Distances in TiMCM-41 by Pulsed EPR Relaxation Enhancement Method

Tatyana A. Konovalova,[†] Shenggang Li,[†] Nikolay E. Polyakov,[‡] A. Ligia Focsan,[†] David A. Dixon,[†,*] and Lowell D. Kispert[†,*]

Department of Chemistry, Shelby Hall, Box 870336, The University of Alabama, Tuscaloosa, Alabama 35487, and Institute of Chemical Kinetics and Combustion, Novosibirsk 630090, Russia

Received: December 23, 2008; Revised Manuscript Received: March 26, 2009

Interspin distances between the Ti^{3+} ions and the carotenoid radicals produced inside TiMCM-41 pores by photoinduced electron transfer from 7′-apo-7′-(4-carboxyphenyl)-β-carotene (coordinated to Ti^{3+}), canthaxanthin (formed as a random distribution of isomers), and β-ionone (model for a short-chain polyene) to Ti^{3+} framework sites were determined using the pulsed EPR relaxation enhancement method. To estimate the electron transfer distances, the temperature dependence of relaxation rates was analyzed in both siliceous and metal-substituted siliceous materials. The phase memory times, T_M, of the carotenoid radicals were determined from the best fits of two-pulse ESEEM curves. The spin−lattice relaxation times, T_1, of the Ti^{3+} ion were obtained from the inversion recovery experiment with echo detection on a logarithmic time scale in the temperature range of 10−150 K. The relaxation enhancement for the carotenoid radicals in TiMCM-41 as compared to that in MCM-41 is consistent with an interaction between the radical and the fast relaxing Ti^{3+} ion. For canthaxanthin and β-ionone, a dramatic effect on the carotenoid relaxation rate, $1/T_M$, occurs at 125 and 40 K, respectively, whereas for carboxy-β-carotene $1/T_M$ increases monotonically with increasing temperature. The interspin distances for canthaxanthin and β-ionone were estimated from the $1/T_M - 1/T_{M0}$ difference, which corresponds to the Ti^{3+} contribution at the temperature where the maximum enhancement in the relaxation rate occurs. Determination of the interspin distances is based on calculations of the dipolar interaction, taking into consideration the unpaired spin density distribution along the 20-carbon polyene chain, which makes it possible to obtain a fit over a wider temperature interval. A distribution of the interspin distances between the carotenoid radical and the Ti^{3+} ion was obtained with the best fit at ∼10 Å for canthaxanthin and β-ionone and ∼9 Å for 7′-apo-7′-(4-carboxyphenyl)-β-carotene with an estimated error of ±3 Å. The interspin distances do not depend on $1/T_M - 1/T_{M0}$ for carboxy-β-carotene which shows no prominent peak in the relaxation rate over the temperature range measured.

Introduction

Photoinduced electron transfer in heterogeneous matrices has been extensively studied for the development of artificial photoredox systems for solar energy conversion and storage.[1−4] Efficient artificial photoredox systems for storing light energy must be able to minimize back electron transfer. The back electron transfer rate is retarded in heterogeneous systems compared to homogeneous solutions.[5] Mesoporous materials, such as MCM-41, containing well-organized nanometer-sized channels, have been found to be good photoredox systems with long-lived photoinduced charge separation for bulky organic and biomolecules.[6−8]

In the current work, we describe our studies of the electron transfer reactions of carotenoids embedded in MCM-41 and TiMCM-41 mesoporous inorganic materials. Electron transfer reactions of carotenoids in such mesoporous materials mimic electron transfer across biological membranes with embedded carotenoids.[9−11] Although the MCM-41 framework itself can act as an electron acceptor, replacement of some tetrahedral Si(IV) atoms in the MCM-41 framework by metal ions such as Al^{3+}, Ti^{4+}, and Mn^{2+} can be used to introduce active sites into this framework.[12−14] It has been reported that the Ti(IV) sites in TiMCM-41 are significantly stronger electron acceptors than the Si(IV) sites,[15−18] and titanosilicate molecular sieves are excellent catalysts for the selective oxidation of various organic substances.[19] X-ray absorption near-edge structure (XANES) and extended X-ray absorption fine structure (EXAFS) data indicate that the Ti(IV) sites in these materials are highly dispersed and in tetrahedral coordination.[20] Diffuse reflectance UV−visible spectra with absorption at 210−230 nm indicate the presence of isolated Ti(IV) site in both tetrahedral and octahedral coordinations.[21] Electron paramagnetic resonance (EPR) and electron spin echo envelope modulation (ESEEM) studies provide convincing evidence for isomorphous substitution of Ti(IV) in the framework of titanosilicate molecular sieves.[22−26]

The long-lived charge-separation feature that was established between carotenoid radicals and the TiMCM-41 framework electron acceptor sites[27] makes this system a potential photoredox system. Therefore, understanding how far an electron can be transferred in this system until it is stabilized on a carotenoid forming a radical (e.g., the distance between the carotenoid radical and the framework acceptor site) is of fundamental importance. In the current study, we determined spin−spin distances between a Ti^{3+} framework ion and a carotenoid radical in TiMCM-41 by analyzing the enhancement in carotenoid radical relaxation rates caused by the metal ion. 7′-Apo-7′-(4-

* To whom correspondence should be addressed. E-mail: dadixon@bama.ua.edu (D.A.D.), lkispert@bama.ua.edu (L.D.K.).
[†] The University of Alabama.
[‡] Institute of Chemical Kinetics and Combustion.

10.1021/jp811369h CCC: $40.75
Published on Web 06/03/2009

carboxyphenyl)-β-carotene (**1**) with a terminal $-CO_2H$ group was selected for the study because carboxyl anions are known to coordinate to Ti cation centers. Canthaxanthin (**2**) was selected because **2** was shown to exhibit no significant interaction with the Ti(IV) site in TiMCM-41,[27] whereas **1** with a terminal $-CO_2H$ group was expected to interact strongly with Ti sites. Infrared measurements have demonstrated that carboxylic acid groups can chemically bind to surface Ti atoms.[28−30] This type of coordination enables an EPR detectable Ti^{3+} concentration to form. No such coordination exists for canthaxanthin (**2**). In the absence of strong coordination, the Ti^{3+} ions cannot be observed by EPR because of reversible electron transfer in the matrix above 77 K. Our previous EPR results demonstrated that the reversible electron transfer occurs between β-carotene and Cu(II) in Cu(II)MCM-41.[31] UV photolysis of this system produces the $Car^{\bullet+}\cdots Cu(I)$ species at 77 K and by temperature cycling to room temperature, the $Car\cdots Cu(II)$ species can be formed.[31] HPLC analysis of the carotenoids isolated from MCM-41 or metal-substituted MCM-41always shows a distribution of carotenoid isomers which demonstrates that electron transfer to the MCM-41 matrix is followed by rapid back electron transfer from the matrix. It has been shown[32] that isomerization of the carotenoid occurs through the formation of radical cations by the following mechanism:

$$\textit{trans}\text{-Car} \rightarrow \textit{trans}\text{-Car}^{\bullet+} + 1e^- \quad (1a)$$

$$\textit{trans}\text{-Car}^{\bullet+} \rightarrow \textit{cis}\text{-Car}^{\bullet+} \quad (1b)$$

$$\textit{cis}\text{-Car}^{\bullet+} + 1e \rightarrow \textit{cis}\text{-Car} \quad (1c)$$

Canthaxanthin (**2**) was chosen because the HPLC analysis of **2** in TiMCM-41 showed a more random distribution of isomers compared to that of β-carotene.[32] HPLC measurements showed that upon isomerization of β-carotene in TiMCM-41 only the 13-*cis* isomer in the ratio of 0.64 to *all trans* was found. Molecular mechanics calculations[32] suggested that this is due to the preferred orientation of the 13-*cis* isomer of β-carotene located around the neck of the MCM-41 pore. Isomerization of **2** in TiMCM-41 produces a mixture of 9-*cis* (9-*cis*/*all trans* = 0.55) and 13-*cis* (13-*cis*/*all trans* = 0.24) isomers with a small amount of 15-*cis* and 9,13-*dicis* isomers. This large difference was another reason why we chose to study canthaxanthin.

β-Ionone was selected to examine the effect on relaxation of a rapidly tumbling molecule with rotating methyl groups in the MCM-41 matrix. Previous relaxation studies have been reported for small molecules.[33] It also provides a means to test the modifications of the equations used to analyze the relaxation phenomena that were needed due to the unpaired spin density being distributed over a long carotenoid polyene chain. Furthermore, it is known that the methyl groups along the polyene chain of the carotenoid radical cation, where the unpaired density is located, undergo rapid rotation even at 5 K as evidenced by no broadening of the EPR lines and recorded ENDOR lines occurring at 5 K. This special feature of carotenoid radicals can simplify the analysis of the relaxation data.

Experimental and Computational Details. ***Sample Preparation.*** Canthaxanthin (**2**) was obtained from Fluka. 7′-Apo-7′-(4-carboxyphenyl)-β-carotene (**1**) was prepared from 8′-apo-β-carotene-8′-al (Roche Vitamins and Fine Chemicals) by base hydrolysis of the corresponding methyl ester, which was obtained by a Wittig reaction with the in situ generated ylide of triphenyl(4-methoxycarbonylbenzyl)phosphonium bromide. β-Ionone (95%) was purchased from Aldrich. The solvent, anhydrous dichloromethane, was obtained from Aldrich. Carotenoid and β-ionone solutions in CH_2Cl_2 (10^{-4} M) were degassed before use by three freeze−pump−thaw cycles. The solvent was evaporated under reduced pressure, and the tube was evacuated and sealed.

Molecular Sieves. Ti(IV)-MCM-41 was synthesized according to the procedure previously described.[34] The concentrations of Ti, Si, and O atoms were 0.001, 0.03, and 0.06 mM/mg, respectively. The average pore size of the calcinated MCM-41 (38 Å) was estimated from powder X-ray diffraction (XRD) analysis according to the procedure described previously.[35] TiMCM-41 showed the same XRD pattern as MCM-41, indicating that the substitution of Ti(IV) into the MCM-41 framework does not alter the structure of the material. MCM-41 and TiMCM-41 samples were activated by heating at 360°C for 12 h in air in a quartz EPR tube before use to remove water molecules and OH^- ions adsorbed on the surface, cooled to room temperature, and then the carotenoid solution was added to the sample in the presence of an inert gas. The sample contained approximately 0.2 mL of carotenoid solution (10^{-4} M) and 20 mg of TiMCM-41 (surface area $\sim$ 1000 m^2/g).[34] Therefore, each sample contained 10^{-8} M (6×10^{15} spins or 3.3×10^{15} m^2/spin) of carotenoid. Assuming that carotenoid locates inside the TiMCM-41 pore of 38 Å diameter, a volume to surface ratio $V/S = 19$ Å was estimated. The volume of the sample was estimated to be 20 $m^2 \times 19$ Å $= 0.04$ cm^3, which gives a carotenoid concentration in the pore of 10^{-8} M/0.04 $cm^3 = 2.5 \times 10^{-4}$ M.

The samples were irradiated at 77 K with a Xe/Hg lamp (1 kW) equipped with a Kratos monochromator (365 nm).

EPR Measurements. Pulsed EPR experiments were performed with a Bruker ELEXSYS E-680 W/X FT/CW Pulse X-band spectrometer equipped with a MD5EN-W1 dielectric resonator, an Oxford Instruments CF935 helium cryostat, and electrically controlled Oxford helium transfer line. The spectrometer is controlled through a Linux workstation with Xepr, the data acquisition and spectral manipulation/analysis software from Bruker.

Microwave pulses were applied with a TWT (1 kW) amplifier. The length of the $\pi/2$ pulse was nominally 16 ns because the concentrations of the spins will not lead to instantaneous diffusion. Phase memory times (T_M) were measured using the two-pulse electron spin echo envelope modulation (ESEEM) sequence ($\pi/2-\tau-\pi-\tau-$echo). Electron spin−lattice times (T_1) were measured with the picket-fence pulse sequence ($\pi-\tau_{pf}-\pi-\tau_{pf}...\pi-T-\pi/2-\tau-\pi-$echo) containing 10 π pulses of 32 ns. An interpulse time τ of 240 ns was used. Pulsed electron−nuclear double resonance (ENDOR) measurements were performed with a Bruker E-560 pulsed ENDOR accessory, a Bruker MD5EN-W1 pulsed ENDOR probe head and an A-500 RF power amplifier using the Davies ($\pi-T-\pi/2-\tau-\pi-\tau-$echo) and Mims ($\pi/2-\tau-\pi/2-T-\pi/2-\tau-$echo) sequences where the additional rf π-pulse was applied during separation time T.[36] Two-dimensional (2D) hyperfine sublevel correlation spectroscopy (HYSCORE) was used with a sequence of four microwave pulses ($\pi/2-\tau-\pi/2-t_1-\pi-t_2-\pi/2-\tau-$echo) and phase cycling to remove additional unwanted echoes and free induction decay signals. The HYSCORE data were taken with nominal pulse widths of 16 ns for the $\pi/2$ pulse, 24−32 ns for the π pulse, and 32 ns for the inversion pulse. The real part of the signal was used after baseline correction followed by zero-filling to 1024 points and then hamming in both

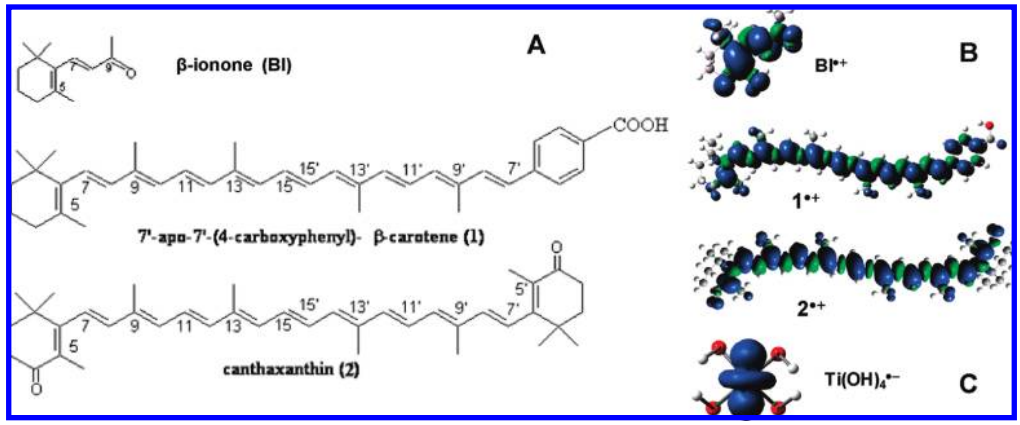

Figure 1. (A) Molecular structures of β-ionone (BI), 7′-apo-7′-(4-carboxyphenyl)-β-carotene (**1**), and canthaxanthin (**2**); and (B) unpaired electron spin densities of their radical cations (*all-trans* for **1** and **2**) and (C) that for $Ti(OH)_4^-$ all calculated at the B3LYP/6-31G** level.

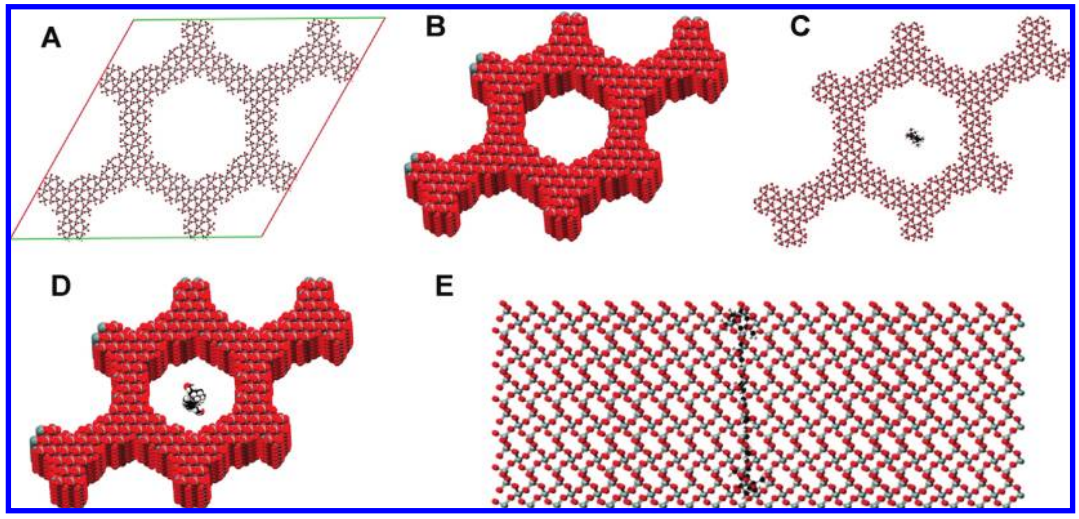

Figure 2. (A) Molecular structure of MCM-41 with a pore diameter of ~38 Å, a distance of ~48 Å between adjacent pore centers, and an average pore wall thickness of ~10 Å. (B) Spacefill view for (A). (C) The structure of MCM-41 with *all-trans* canthaxanthin (**2**) inserted vertically through the pore. (D) Spacefill view for (C). (E) Side view for (C).

directions before Fourier transformation. The displayed spectra are the magnitudes of the complex Fourier transformed data sets.

Pulsed ENDOR spectra were simulated by using the SimBud program which provides spectral simulations at various time delays.[37]

Density Functional Theory (DFT) Calculations. All DFT calculations were done with the Gaussian 03 program package[38] on the Cray XD1 computer at the Alabama Supercomputer Center. Geometries were optimized at the DFT level with the B3LYP exchange-correlation functional[39] and the 6-31G** basis set,[40] which has been shown to yield reasonable geometries for β-carotene-based radicals.[41] Single-point calculations at these geometries were carried out to predict ENDOR and 2D-HYSCORE hyperfine couplings (hfc) at the B3LYP level with the VTZP basis set from the Ahlrichs group.[42] This basis set has been shown to give good NMR chemical shifts[43] and good EPR parameters for carotenes.[41] The unpaired electron spin densities were plotted using the AGUI program[44] from the wave functions and spin densities from the DFT calculations. The spin density is defined as the difference in the alpha and beta spin densities.

Results and Discussion

Molecular Structures. Molecular structures together with the DFT unpaired electron spin density distributions in the radical cations $BI^{\bullet+}$, $\mathbf{1}^{\bullet+}$ and $\mathbf{2}^{\bullet+}$ are shown in Figure 1. For $\mathbf{1}^{\bullet+}$ and $\mathbf{2}^{\bullet+}$, the spin densities are more or less equally distributed across the π system. Also shown in Figure 1 is the molecular structure and unpaired electron spin density for the $Ti(OH)_4^-$ ion, where the unpaired electron is localized on the Ti(III) atom.

Figure 2A,B shows the molecular structure of MCM-41 with a pore diameter of ~38 Å built from the bulk structure of α-quartz[45] using a similar procedure by Jentys and co-workers.[46] A template of the size 95 Å × 95 Å × 11 Å along the **a**, **b**, **c** directions was used for creating the unit cell structure for MCM-41. The pore is approximately hexagonal. The distance between the adjacent pore centers is ~48 Å, and the wall thickness of the pore is ~10 Å. As shown in Figure SM-1(A,B) in Supporting Information, the *all-trans* structures of the carotenoid molecules with a chain length of 25−30 Å can barely fit in the MCM-41 pore of this size if they are placed across the pore. They can, however, readily diffuse if arranged vertically in the MCM-41 cylindrical pores (Figure 2C−E). The 13-*cis* structures of the carotenoids fit much better than the *all-trans* and 9-*cis* structures when placed across the pore (Figure SM-1(B,C,D) in Supporting Information).

EPR Measurements. Carotenoid (**1**) embedded in both MCM-41 (Figure 3, dotted line) and TiMCM-41 produces an EPR signal with $g = 2.0028 \pm 0.0002$, which is characteristic of carotenoid radical cation ($Car^{\bullet+}$)[47,48] before irradiation. EPR detectable concentrations of β-ionone (BI) and carotenoid (**2**)

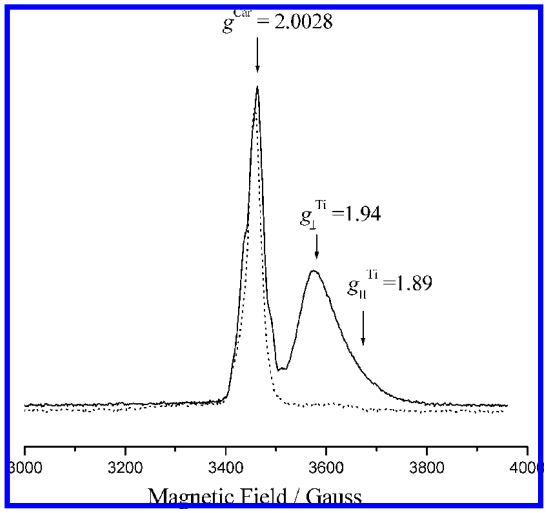

Figure 3. Two-pulse echo induced EPR field sweep of 7′-apo-7′-(4-carboxyphenyl)-β-carotene (**1**) in MCM-41 (dotted line) and Ti-MCM-41 (solid line). EPR parameters: B = 3456 G; ν = 9.710 978 GHz; τ = 200 ns; SRT = 6 ms; T = 20 K.

radicals in both matrices were achieved after visible light ($\lambda \geq$ 350 nm) irradiation. Besides the $Car^{\bullet+}$ signal, the EPR spectrum of (**1**) in TiMCM-41 exhibits an additional signal with $g_{\perp}$ = 1.94 and $g_{||}$ = 1.89 (Figure 3, solid line). An EPR signal with similar axial **g** tensor, $g_{\perp}$ = 1.971 and $g_{||}$ = 1.901, has been observed after γ-irradiation of Ti(IV)MCM-41 and assigned to Ti(III) produced by the reduction of Ti(IV) at a framework tetrahedral site.[24] The slightly different **g** tensor observed in this study could be due to the interaction of Ti^{3+} ions with absorbed carotenoid molecules. It has been reported that incorporation of CO, D_2O, NH_3, and CD_3OH in Ti-containing mesoporous materials changes the Ti^{3+} **g** tensor parameters from the original Ti^{3+} observed in the absence of these adsorbates.[22−24] No Ti^{3+} signal was detected for the canthaxanthin (**2**)/TiMCM-41 sample.

The calculated hyperfine couplings (hfc) by the DFT method can be used to assign the experimental isotropic hfcs as shown in Table 1. Many of the hfcs for (**1**) can be assigned to the radical cation. It is also possible to assign a number of the remaining hfcs to the lowest energy structure of the radical generated by loss of a proton from position 4 of the radical cation. The irradiation introduces enough energy into the system to form higher energy radicals and we can assign additional hfcs to the radicals generated by loss of a proton from position 9′ (4.6 kcal/mol above position 4) and from position 5 (4.8 kcal/mol above position 4). It is possible that even higher energy neutral radicals may be present (see Supporting Information) but they are not needed in making the assignments. For **2**, only a few of the hfcs could be assigned to the radical cation. Most of the spectral lines appear to be due to the lowest energy radical generated by loss of a proton from position 5 of the radical cation. The smallest hfc can be assigned to the higher energy radical cations generated by loss of a proton from position 9 (4.3 kcal/mol above position 5) and from position 13 (5.8 kcal/mol above position 5).

Pulsed ENDOR and HYSCORE Measurements. To prove the formation of similar carotenoid radical species in both silicious and Ti(IV)-substituted matrices, the hyperfine coupling constants (hfc) were determined from the analysis of their pulsed ENDOR and 2D HYSCORE spectra. ^{1}H ENDOR spectra of the Davies and Mims pulse sequences[36] were measured for the radicals derived from **1** and **2** in MCM-41 and TiMCM-41

TABLE 1: Proton Isotropic Hyperfine Couplings (Hfc) in MHz of (1) and (2) Determined from Pulsed (Mims and/or Davies) ENDOR/HYSCORE Analysis in MCM-41 and TiMCM-41 and DFT Calculations[a]

MCM-41 ENDOR/HYSCORE	TiMCM-41 ENDOR/HYSCORE	assignment	DFT
	Carboxy-β-carotene (**1**)		
±0.32/−	±0.3−0.4/−	$Car^{\bullet+}$/C(3)H_α	−0.20
		$Car^{\bullet+}$/C(10)H_α	0.48
±1.02, ±1.22/−	±1.02, ±1.22/−	$Car^{\bullet+}$/C(2′)H_α	1.05
		#Car•(4)/C(2′)H_α	1.15
		#Car•(4)/C(4′)H_α	1.16
−/−	±2.20/−	$Car^{\bullet+}$/C(8)H_α	2.54
		$Car^{\bullet+}$/C(5′)H_α	−2.47
		$Car^{\bullet+}$/C(1′)H_α	−2.43
		#Car•(4)/C(5′)H_α	−2.72
		#Car•(4)/C(1′)H_α	−2.65
±3.24/−	−/−	$Car^{\bullet+}$/C(13)CH_3	3.24
		$Car^{\bullet+}$/C(14)H_α	−3.29
		$Car^{\bullet+}$/C(10′)H_α	3.18
		$Car^{\bullet+}$/C(12′)H_α	3.43
±4.62/−	±4.40/−	#Car•(9′)/C(8)H_α[b]	4.45
−/−	±5.70/−	#Car•(4)/C(9)CH_3	5.32
±7.50/−	−/−	$Car^{\bullet+}$/C(9)CH_3	7.50
		$Car^{\bullet+}$/C(5)CH_3	7.81
		#Car•(4)/C(11)H_α	7.69
−/−	±11.20−	#Car•(9′)/C(7)H_α[b]	−10.85
		#Car•(5)/C(10)H_α[c]	−10.80
	Canthaxanthin (**2**)		
±1.20, ±1.50/−	±1.50/−	#Car•(9)/C(7)H_α[d]	1.65
		#Car•(13)/C(9)CH_3[e]	−1.34
±2.05, ±2.10/−	±2.00/−	#Car•(5)/C(2)H_α	2.28
		#Car•(5)/C(5)CH_3	−2.46
±3.00/−	±3.00/−	$Car^{\bullet+}$/C(10)H_α	2.82
		$Car^{\bullet+}$/C(10′)H_α	2.83
		$Car^{\bullet+}$/C(15)H_α	−3.21
		$Car^{\bullet+}$/C(15′)H_α	−3.25
±7.20/−	±7.30/−	#Car•(5)/C(11)H_α	7.10
±7.50/±7.49	±7.60/−	#Car•(5)/C(13)CH_3	−7.55
±8.10/−	−/−	#Car•(5)/C(12′)H_α	8.61
±8.60/±8.60	±8.70/±8.70	$Car^{\bullet+}$/C(11)H_α	−8.78
		$Car^{\bullet+}$/C(11′)H_α	−8.82
−/±9.06	−/−	$Car^{\bullet+}$/C(9)CH_3	9.34
		$Car^{\bullet+}$/C(9′)CH_3	9.36
		#Car•(5)/C(8)H_α	−9.36
−/±9.70	−/−	#Car•(5)/C(8)H_α	−9.99
		#Car•(5)/C(14′)H_α	9.60
		#Car•(5)/C(15)H_α	9.57
±11.70/±11.80	−/−	#Car•(5)/C(10)H_α	−11.87
±13.50/±13.70	±13.50/±14.10	#Car•(5)/C(12)H_α	−13.67
±14.50/−	±14.60/−	#Car•(5)/C(11′)H_α	−14.68

[a] B3LYP/VTZP (Ahlrichs)//B3LYP/6-31G**. For further details see ref 93. [b] 4.6 kcal/mol higher in energy than the ground state of the radical #Car•(4). [c] 4.8 kcal/mol higher in energy than the ground state of the radical #Car•(4). [d] 4.3 kcal/mol higher in energy than the ground state of the radical #Car•(5). [e] 5.8 kcal/mol higher in energy than the ground state of the radical #Car•(5).

(Figures 4 and 5). Pulsed ENDOR spectra were measured at different delay time τ to avoid the "blind-spot" effect (ENDOR amplitude = 0), periodic oscillations of the ENDOR response that is proportional to $1 - \cos(2\pi A_i \tau)$.

The ENDOR spectra were simulated using the SimBud program which allows simulations at different time delays τ.[37] Isotropic methyl (β) proton hfcs determined from the ENDOR spectral simulations are listed in Table 1. Usually, the β-protons have very little anisotropy and give rise to narrow and intense lines in powder ENDOR spectra whereas lines from α-protons are often broadened and not easily detected.[49] HYSCORE measurements were carried out to determine accurately the α-proton couplings of the carotenoids. Figure 6 shows contour plots of the 2D HYSCORE spectra with "skyline projections" for **2** in MCM-41 (A) and TiMCM-41(B). For powder spectra where considerable anisotropic hyperfine interactions are present,

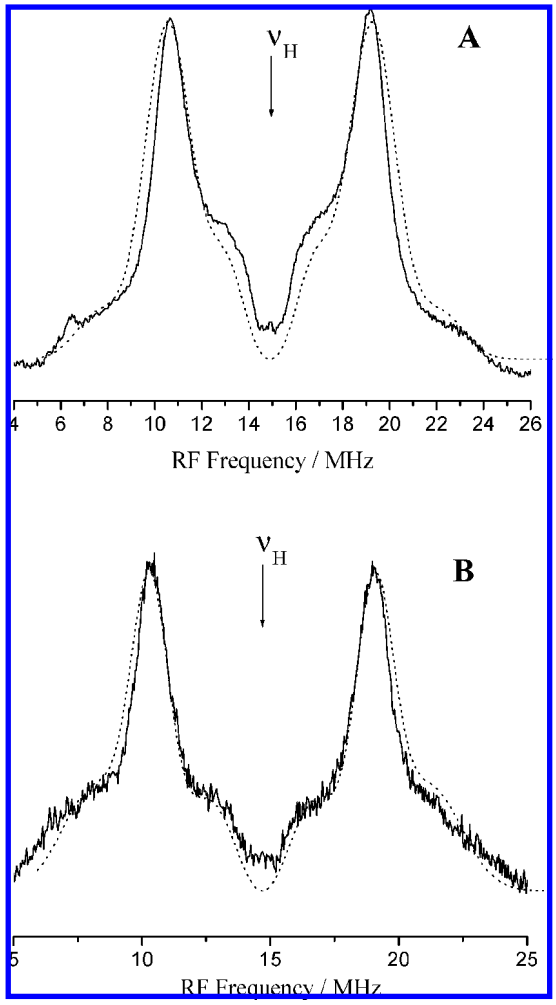

Figure 4. Proton Davies ENDOR of canthaxanthin (**2**) in MCM-41 (A) and Ti-MCM-41 (B). Parameters: $B = 3499$ G; $\nu = 9.8183$ GHz; $T = 9$ K; $\tau = 200$ ns; SRT = 5999 μs; rf π pulse = 8000 ns. Solid line, experimental; dotted line, simulated with isotropic hfc of 3.0, 8.6, 14.5 MHz (A) and 3.0, 8.7, 13.0 MHz (B).

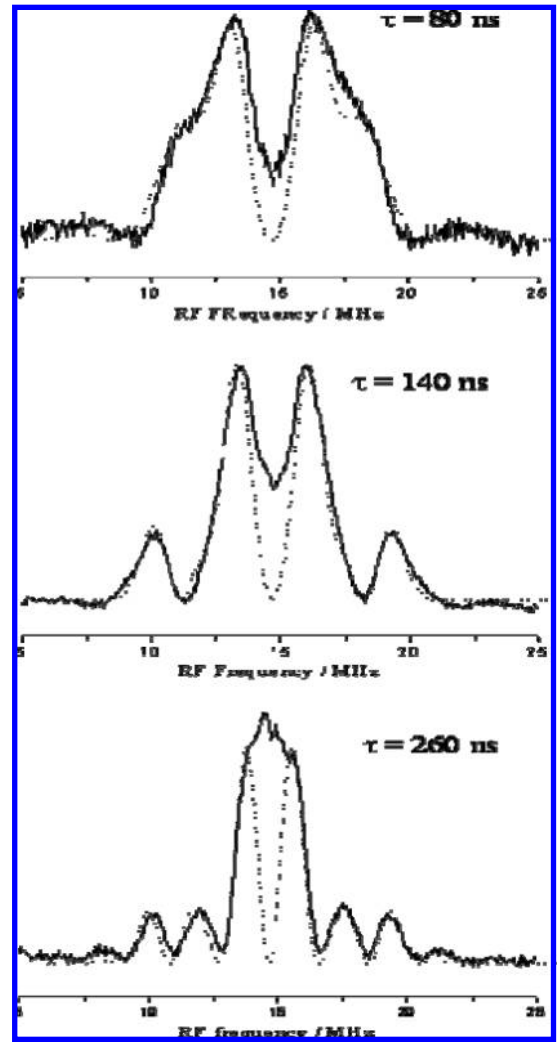

Figure 5. Proton Mims ENDOR of canthaxanthin (**2**) in Ti-MCM-41. Parameters: $B = 3454$ G; $\nu = 9.6898$ GHz; $T = 20$ K; number of points = 512; SRT = 8 ms; rf π pulse = 8000 ns measured at different time delays τ. Solid line, experimental; dotted line, simulated using the following hfc: 2.0, 7.3, 13.5 MHz for $\tau = 80$ ns; 2.0, 7.6 MHz for $\tau = 140$ ns; 1.5, 8.7 MHz for $\tau = 260$ ns.

the cross peaks are elongated and become ridges.[50,51] Ridges centered at the ^{1}H free Larmor frequency are due to the carotenoid protons. A peak at 2.9 MHz is attributed to the ^{29}Si matrix nuclei at the vicinity of the unpaired electron.

The α-proton hyperfine tensors of carotenoids appear to be rhombic which is characteristic of planar conjugated radicals with the unpaired spin density in a p_Z orbital of the carbon with a C−H group. Such tensors can be determined from the HYSCORE analysis of the contour line-shapes of the cross peaks according to the procedure described by Dikanov et al.[50,52,53] The complete hyperfine tensor is extracted from a linear fit of the cross-peak coordinates in a ν_α^2 vs ν_β^2 plot where the ridges become straight lines and each pair of outlining ridges should intersect at $|\nu_\alpha \pm \nu_\beta| = 2\nu_1$. Each ridge indicates two of the three principal component of the rhombic hyperfine tensor in the same manner as the ridges from an axial tensor (Figure 7a,b). The third component was determined from the DFT calculations. These findings provided a basis for evaluating the entire hyperfine tensor for the canthaxanthin (**2**) radical.

The isotropic proton hfc determined from the ENDOR and HYSCORE analysis were assigned on the basis of our previous studies.[54−58] As shown in Table 1, similar radical species were produced upon oxidation of the carotenoids in silicious and Ti-containing MCM-41.

Pulsed EPR Relaxation Enhancement Measurements. Carotenoids oxidized in TiMCM-41 represent a system that contains a rapidly relaxing metal ion and a slowly relaxing organic radical. The effect of the rapidly relaxing paramagnetic center on the electron spin relaxation rate of a more slowly relaxing center can be used to determine interspin distances.[59−63] The temperature dependence of relaxation rates has been analyzed to determine distances between an organic radical and a transition metal ion in photosynthetic systems[64−72] and in magnetically dilute solids.[63,73−77]

The effect of a rapidly relaxing framework Ti^{3+} ion on T_1 and T_M of a slowly relaxing carotenoid radical was measured as a function of temperature in both siliceous and Ti-substituted materials. It was found that the phase memory times (Figure 8a), T_M, and spin−lattice relaxation times (Figure 8b), T_1, are shorter for carotenoids embedded in TiMCM-41 than those in siliceous MCM-41. The results show that, in the temperature range of 10−150 K, carotenoid T_M values are of the order of microseconds (0.25−0.5 μs) (Figure 8), which is orders of magnitude shorter than T_1 (0.5−0.7 s). Therefore, contributions to relaxation that are significant with respect to $1/T_1$ for the carotenoid are negligible with respect to $1/T_M$. We analyzed the

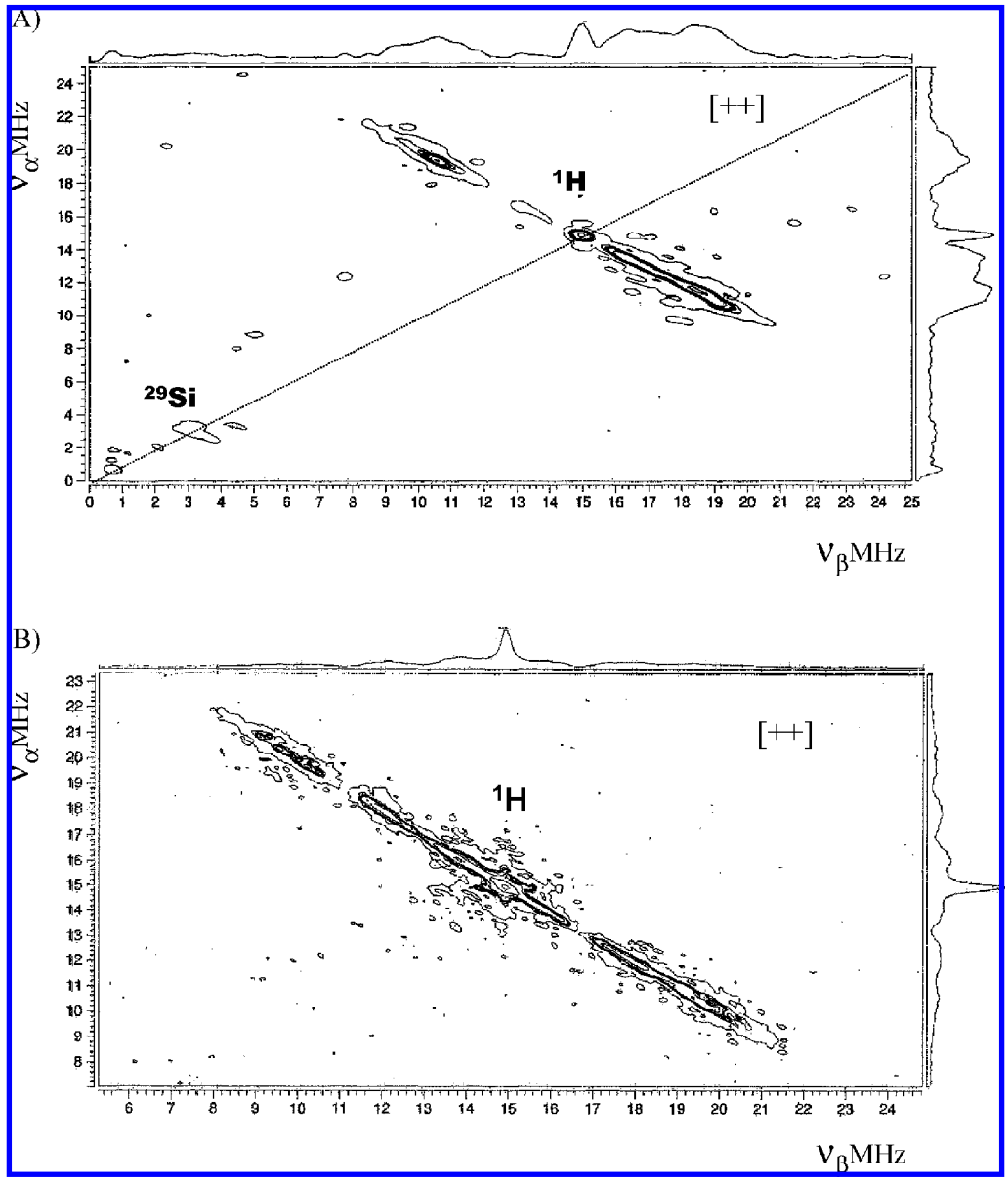

Figure 6. Contour plot of the HYSCORE spectra of canthaxanthin (**2**) in MCM-41 (A) and TiMCM-41 (B). Parameters: $T = 10$ K; $B = 3500$ G; $\nu = 9.8229$ GHz; $\pi/2 = 16$ ns; $\pi = 24-32$ ns; inversion pulse = 32 ns; $\tau = 140$ ns (A) and 180 ns (B); SRT = 4 ms (A) and 5.1 ms (B). The spectra were obtained after Fourier transformation of 2D time-domain patterns containing 256 × 256 points (A) and 324 × 324 points (B) for the data set. Data manipulation before Fourier transformation: baseline correction followed by zero-field filling to 1024 points and Hamming in both directions.

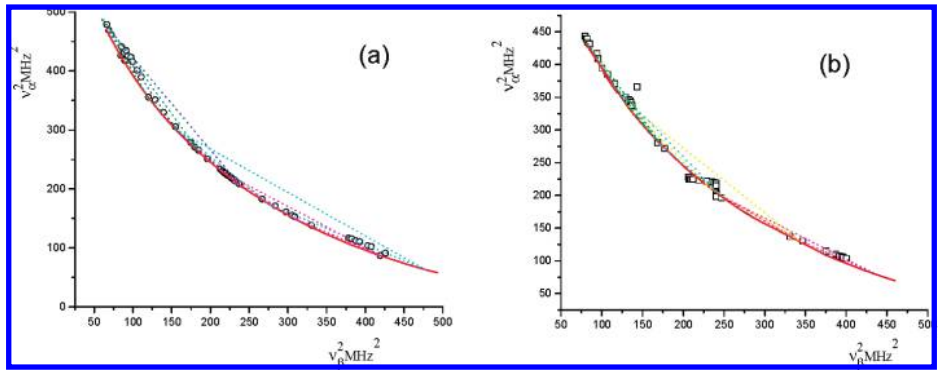

Figure 7. Coordinates of the HYSCORE ridges plotted as the squares of the frequencies for the canthaxanthin (**2**) in MCM-41 (a) and TiMCM-41 (b). The solid curved line corresponds to $\nu_\alpha + \nu_\beta = 2\ \nu_1$, and the straight dotted lines are least-squares fits to the data points.

impact on the carotenoid T_M to ensure that the observed effects are mostly due to interaction with the rapidly relaxing metal ion and not due to some other dynamic effects in the system.

For canthaxanthin (**2**), the two-pulse ESEEM was taken at the maximum of the echo-detected EPR signal of the Car$^{\bullet+}$, because no Ti^{3+} signal was observed in this case. The T_M values

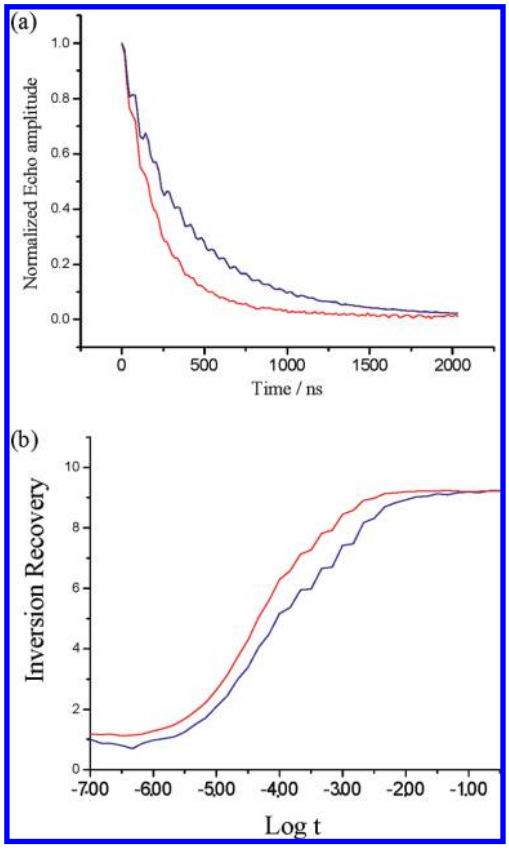

Figure 8. (a) Two-pulse echo decay for canthaxanthin (**2**) in MCM-41 (blue) and Ti-MCM-41 (red). Parameters: $T = 110$ K; $B = 3460$ G; $\nu = 9.7127$ GHz; $\tau = 100$ ns; SRT = 8 ms. (b) Inversion recovery with echo detection on logarithmic time scale for canthaxanthin (**2**) in MCM-41 (blue) and TiMCM-41 (red). Parameters: $T = 70$ K; $B = 3460$ G; $\nu = 9.7127$ GHz; $\pi/2$ (pulse 1) = 16 ns; π (pulse 2) = 32 ns; inversion π pulse = 16 ns; number of π pulses in picket fence = 10; delay after inversion pulse = 100 ns; delay in picket fence = 300 ns; $\tau = 100$ ns; SRT = 500 μs.

were obtained from the two-pulse echo decay fits in the temperature range of 12−155 K.

Dipole−dipole interactions are related to the distance between the interacting spins and to the orientation of the applied magnetic field.[78] Because of the overlapping decay curves for the various orientations of the interspin vector relative to the external magnetic field, the decays could not be fit with single-exponential decays. Indeed, the canthaxanthin (**2**) echo decay curves were best fit by using a double exponential with a slow and a fast component. A single exponential cannot be used because the relaxation is orientationally dependent. The double exponential could also indicate that more than one type of radical species was produced on photoexcitation of the carotenoid. According to our previous results, $Car^{\bullet+}$ is the primary radical species formed by photooxidation of these compounds in MCM-41. DFT calculations from our group show that neutral carotenoid radical formation via the proton loss from the primary $Car^{\bullet+}$ can occur upon UV/visible irradiation.[41,58] Thus, the slow component, which provided the major contribution to the echo amplitude, was attributed to the carotenoid radical cation. The fast component could be due to the neutral carotenoid radical.

The dominant effect of the rapidly relaxing metal spin on the T_M of the slowly relaxing spin is analogous to the effects of a physical motion, such as rotation of the methyl group, which averages nuclear spins to which the unpaired electron is coupled. The most dramatic effect on T_M occurs when the metal relaxation

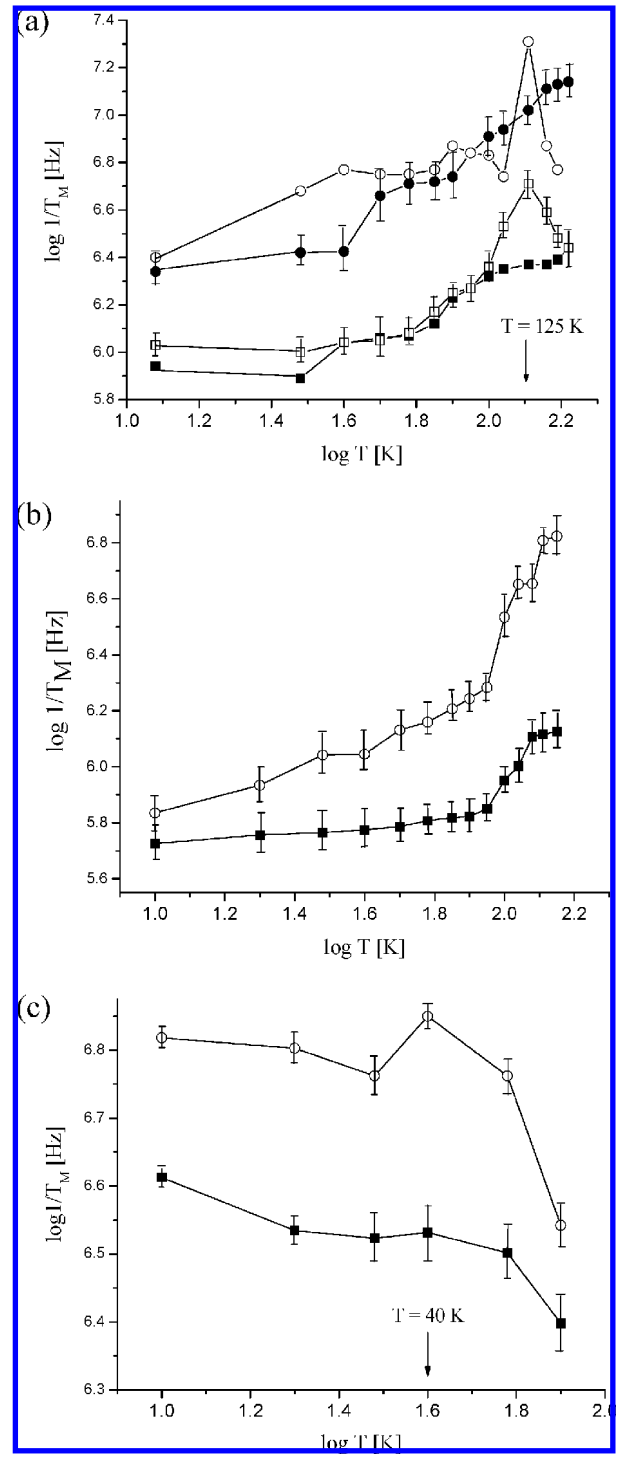

Figure 9. Temperature dependence of $\log(1/T_M)$ (T_M in Hz) (a) for (**2**) radical ESEEM curves were best fitted as double exponentials: (−■−) slow component for Car/MCM-41; (−□−) slow component for Car/TiMCM-41; (−●−) fast component for Car/MCM-41; (-○-) fast component for Car/TiMCM-41; (b) for (**1**) radical. The ESEEM curves were fitted as double exponentials: (−■−) Car in MCM-41; (−○−) Car in TiMCM-41. Two-pulse ESEEM parameters: $B = 3456$ G; $\nu = 9.710\,978$ GHz, $\tau = 100$ ns, SRT = 8 ms, number of points = 512; (c) for β-ionone radical (BI) cation. The ESEEM curves were fitted as double exponentials: (−■−) β-ionone in MCM-41; (−○−) β-ionone in TiMCM-41. Parameters for MCM-41: $B = 3464$ G, $\nu = 9.740\,904$ GHz, $\pi/2$ (pulse 1) = 16 ns, π (pulse 2) = 32 ns, $\tau = 100$ ns.

rate is of the same order of magnitude as the dipolar couplings to the slowly relaxing spin. This phenomenon is shown in Figure 9a which exhibits the logarithmic temperature dependence of

the canthaxanthin (**2**) radical relaxation rate, $1/T_M$, in siliceous and Ti-containing materials. As the temperature increases, the metal relaxation rate increases and becomes comparable to the dipolar splittings at ~125 K. As a result, in TiMCM-41, both the fast and slow components show significant increases in $1/T_M$ around this temperature. The carotenoid radical relaxation rate in siliceous MCM-41 did not depend as strongly on temperature as that in the sample containing Ti^{3+}. Thus, the relaxation enhancement is due to the dipolar interaction with the framework Ti^{3+} ions and not due to the hyperfine interaction as a result of the rotation of the carotenoid methyl groups. A similar dramatic increase in $1/T_M$ has been observed for spin-labeled oxidized cytochrome *c*[79] and for spin-labeled metmyoglobin.[63,74] The relaxation rates of the **2** radical in siliceous MCM-41 ($1/T_{M0}$) and in TiMCM-41 ($1/T_M$) are listed in the Supporting Information.

As the EPR spectrum of 7′-apo-7′-(4-carboxyphenyl)-β-carotene (**1**) incorporated in TiMCM-41 exhibits both carotenoid radical and the Ti^{3+} signals (see Figure 3), the two-pulse echo decay of $\mathbf{1}^{\bullet+}$ was measured at the field position of its maximum absorption, 3456 G. The ESEEM curves were best fitted as double exponentials. Figure 9b shows a significant increase in $1/T_M$ for the (**1**) radical in TiMCM-41 compared to the MCM-41 sample, indicating interaction of the carotenoid with the Ti^{3+} ion. In contrast to canthaxanthin (**2**), the carotenoid (**1**) shows a monotonic increase in the relaxation rate. No prominent peak in the relaxation was observed (Figure 9b).

The T_1 values of Ti^{3+} were determined from the inversion recovery experiment with echo detection in the temperature range of 10−120 K measured at 3582 G, the position of the Ti^{3+} maximum absorption. In Figure SM-4, the echo recovery is plotted against log *t* at different temperatures (10, 30, 50, and 70 K). The relaxation rates for **1** and T_1 for Ti^{3+} are summarized in the Table SM-4.

Figure 9c shows the temperature dependence of $1/T_M$ for β-ionone (BI) in MCM-41 and TiMCM-41. The general decrease in $1/T_M$ with increasing temperature is typical for small radicals where fast motion limit dominates. This is in contrast to the long-chain carotenoids **1** and **2** where the slow motion limit is dominant over the temperature range measured. The T_M values were determined from analysis of the two-pulse ESEEM curves measured at the position of the maximum absorption of the $BI^{\bullet+}$. The curves were best fit as double exponentials. An increase in $1/T_M$ for $BI^{\bullet+}$ in TiMCM-41 compared to that in MCM-41 especially near 40 K was observed. The results are presented in the Supporting Information.

Interspin Distance Determination. The relaxation enhancement displayed in Figure 9 can be analyzed to estimate the organic radical−Ti^{3+} interspin distances. The quantitative analysis of the dipolar relaxation enhancement has been established.[59,60,80−84] Zhidomirov and Salikhov presented the following expression (for the interpretation of ESEEM experiments) for the impact on the echo decay curve of a process called "spectral diffusion" in a spin-coupled system:[80]

$$E(2\tau) = R^{-2}\{\exp(-2\tau/\tau_c)[\tau_c^{-2}\sinh^2(R\tau) + R^2\cosh^2(R\tau) + R\tau_c^{-1}\sinh(2R\tau) + \Delta^2\sinh^2(R\tau)]\} \quad (2)$$

where $E(2\tau)$ is the spin echo intensity as a function of τ, τ is the time between microwave pulses in the two-pulse sequence, τ_c is the correlation time for the dynamic process, Δ is the orientation-dependent spin−spin splitting, which includes the dipolar (D) and exchange (J) contributions, and $R^2 = \tau_c^{-2} - \Delta^2$. It has been proposed[80] that τ_c can be approximated as the T_1 of the fast relaxing spin. "Spectral diffusion" has been defined[84−86] as the fluctuation in the resonant frequency of an individual spin caused by fluctuations in the local field, in this case by changes in the dipolar field at the location of a particular spin, and cross relaxation. The dipolar interactions and the distances can be determined according to procedures described elsewhere,[63,74,75,77,81,83,87] based on the two site-exchange model that includes simulations of the paramagnetic metal ion contribution, W_{dd}

$$\frac{1}{T_M} = \frac{1}{T_{M0}} + W_{dd} \quad (3)$$

where $1/T_M$ and $1/T_{M0}$ are the organic radical relaxation rates in the presence and absence of the metal ion, respectively. W_{dd} can be numerically simulated on the basis of relaxation enhancement in a two-pulse echo, $W(\tau)$, which is due to electron−electron interaction between the two spins. The $W(\tau)$ calculations (see below) were based on numerical integration over the angle between the external magnetic field and the internuclear axis. As discussed below, exchange has been neglected in our approach because of the small amount of excess spin density on any carotene carbon and in this case, $\Delta \sim D$.

In our initial simulations, the experimental curves were fit in the time interval from 100 ns (instrumental dead time) to ~600 ns. We assume that the spin−spin interaction, which gives exponential spin echo decay, contributes most in this time interval. Contributions from other slower processes at longer time intervals cause nonexponential decay, so the slower component was subtracted prior to the simulations. The simulations included $1/T_M - 1/T_{M0}$ of the carotenoid radical and T_1 values of the Ti^{3+} ion (see Figure SM-4 and Table SM-4, Supporting Information). This standard procedure[74,87] allows determination of the distance at the particular temperature where the relaxation rate shows a prominent increase. The distances obtained by using $1/T_M - 1/T_{M0}$ for canthaxanthin (**2**) at 125 K and for β-ionone at 40 K are found to be 13.2 and 10.5 Å, respectively. However, the original method based on the point-dipole approximation cannot be used for carboxy-β-carotene (**1**), because there is no prominent peak in the relaxation rate.

The basic procedure described above assumes a point-dipole model and needs to be modified for a distribution of unpaired spin density along the carotenoid chain as found for carboxy-β-carotene (**1**). Relaxation of the carotenoid (**1**) occurs through several different mechanisms including the dipolar−dipolar interaction. Assuming that k_{dd} is the rate constant of the dipolar−dipolar interaction and $K = (k_1 + k_2 + k_3 + ...)$ is a sum of the rates of all other relaxation pathways, we can extract k_{dd} from eq 4.

$$e^{-k_{dd}(t)} = \frac{e^{-[k_{dd}(t)+K(t)]}}{e^{-K(t)}} \quad (4)$$

Thus, the interspin distance can be derived from the ratio of exponential fits of two-pulse echo decays in the presence and absence of the Ti^{3+} ion. The concentration of the samples under study was low enough ($\sim 10^{-4}$ M) that there was no impact on the spin echo decay from instantaneous diffusion. The spin echo decay simulations were carried out to reproduce the initial ratio of fits in eq 4. The adjustable parameters were the principal components of the dipole interaction tensor. For carotenoids, the distribution of unpaired spin density along the C_{22} polyene

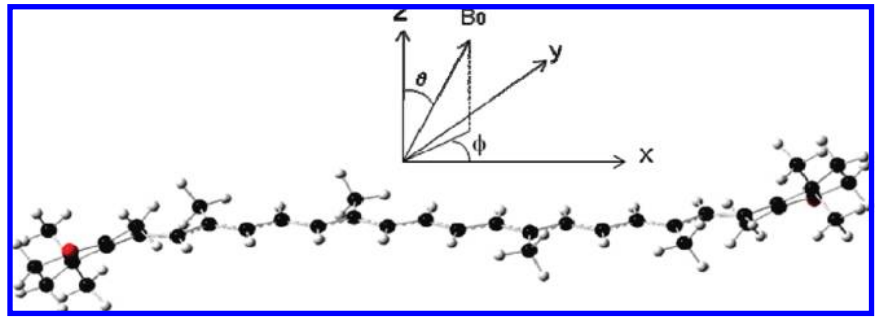

Figure 10. Cartesian coordinate system of canthaxanthin (**2**) radical cation used in Table 2.

TABLE 2: Dipolar Tensor Components B_{aa}, B_{bb}, and B_{cc} (in MHz) Determined Using a ^{3}He/Car$^{\bullet+}$ Model Calculated at the B3LYP/6-31G Level and the Scaled Values for the Ti^{3+} Ion Interacting with the Organic Radical**

cooordinates (Å)							
x	*y*	*z*	$B_{aa}(^3He)$	$B_{bb}(^3He)$	$B_{cc}(^3He)$	$B_{aa}(Ti^{3+})$	$B_{cc}(Ti^{3+})$
Canthaxanthin (**2**) Radical Cation							
0	0	3	0.454	0.059	−0.513	385.9	−436.05
0	0	5	0.152	0.009	−0.161	129.2	−136.85
0	0	7	0.074	0.011	−0.085	62.9	−72.25
0	0	9	0.043	0.011	−0.053	36.55	−45.05
0	0	11	0.027	0.009	−0.036	22.95	−30.6
0	0	13	0.018	0.008	−0.026	15.3	−22.1
0	0	15	0.013	0.007	−0.019	11.05	−16.15
0	3	0	0.420	0.008	−0.428	357.0	−362.8
0	7	0	0.079	0.015	−0.094	67.15	−79.9
0	11	0	0.028	0.010	−0.038	23.8	−32.3
0	15	0	0.013	0.007	−0.020	11.05	−17.0
0	2.1	2.1	0.494	0.069	−0.563	419.9	−478.55
0	4.9	4.9	0.077	0.011	−0.089	65.45	−75.65
0	7.8	7.8	0.027	0.009	−0.036	22.95	−30.6
0	10.6	10.6	0.013	0.007	−0.020	11.05	−17.0
5	0	7	0.080	0.020	−0.101	68.0	−85.85
5	0	11	0.027	0.012	−0.039	22.95	−33.15
10	0	7	0.071	0.038	−0.109	60.35	−92.65
10	0	11	0.024	0.015	−0.039	20.4	−33.15
15	0	7	0.037	0.030	−0.066	31.45	−56.1
15	0	11	0.015	0.013	−0.028	12.75	−23.8
Carboxy-β-carotene (**1**) Radical Cation							
0	0	3	0.424	0.049	−0.474	363.7	−406.6
0	0	5	0.144	0.006	−0.150	123.5	−128.7
0	0	7	0.071	0.009	−0.080	60.35	−68.0
0	0	9	0.041	0.009	−0.050	34.85	−42.5
0	0	11	0.026	0.009	−0.035	22.1	−29.75
0	0	13	0.018	0.007	−0.025	15.3	−21.25
0	0	15	0.012	0.006	−0.019	10.2	−16.15

chain results in a small fraction of an electron (approximately 0.05) at each carbon which makes exchange interaction (*J*) small. The values of the principal components of the dipole interaction tensor were calculated at the B3LYP/6-31G** level using a model system consisting of a carotenoid radical cation interacting with a ^{3}He atom; the ^{3}He was placed at different distances and orientations with respect to the carotenoid radical (see Table 2 and Figure 10). The dipolar interaction values were recalculated for Ti^{3+} using the ratio of the magnetic moments $\mu^{Ti(III)}/\mu^{3He} \sim 850$.[88] The calculated principal components of the dipole interaction tensor for the carotenoid are predicted to have near-rhombic symmetry rather than the axial symmetry expected for the interaction of two point spins, for example, the interaction of ^{3}He with the CH_3 radical. The values of the principal components and thus the distances and directions between the two electron spins were determined by matching the simulations with fits of the experimental echo decay curves.

The spin echo decay quantity $W(\tau)$ is similar to $E(2\tau)$ from eq 2 and is used to interpret spin relaxation experiments. Equation 5 follows from eq 2[75,80]

$$W(\tau) = \frac{1}{4\pi}\exp\left(-\frac{\tau}{T_1}\right)\int_0^{2\pi}\int_0^{\pi}\sin\theta\,d\theta\,d\phi\left\{\left[\cosh(R\tau) + \frac{\sinh(R\tau)}{2RT_1}\right]^2 + \frac{D^2}{4R^2}\sinh^2(R\tau)\right\} \quad (5)$$

with $\tau_c = T_1$. Equation 5 is specialized for a powder sample of weakly coupled pairs of spins where the spin−spin interaction has a time dependence driven by the T_1 of one of the interacting spins, usually the fast one. With $\Delta \sim D$ and $T_1 \sim \tau_c$, $W(\tau)$ is then integrated over all orientations by numerical integration over θ, the angle between the external magnetic field and the internuclear axis, and ϕ, the angle between the magnetic field and the carotenoid polyene chain plane (Figure 10), at any given instant τ. In eq 5, D and R were calculated from eqs 6 and 7:

$$D(r,\theta,\phi) = a(r)\sin^2\theta(\cos^2\phi - \sin^2\phi) + c(r)(\cos^2\theta - \sin^2\theta\sin^2\phi) \quad (6)$$

$$4R^2 = T_1^{-2} - D^2 \quad (7)$$

where T_1 is the longitudinal relaxation time of the fast relaxing Ti^{3+} ion, D is the dipole−dipole interaction between the slow relaxing organic radical and the fast relaxing Ti^{3+} ion, r is the interspin distance, and θ and ϕ are the angles between the direction of the external magnetic field and a vector connecting the two spins. Equation 5 can be evaluated as a function of r, the distance between the spins. If the principal components have axial symmetry, i.e., $b = a$ and $c = -2a$, eq 6 reduces to

$$D(r,\theta) = a(r)(1 - 3\cos^2\theta) \quad (8)$$

and the integration in eq 5 is one-dimensional in θ. For the interaction between the carotenoid radical cation and Ti^{3+}, the principal components have near-rhombic symmetry, i.e., $b = 0$ and $c = -a$ (Table 2) and eq 6 reduces to

$$D(r,\theta,\phi) = a(r)(\sin^2\theta\cos^2\phi - \cos^2\theta) \quad (9)$$

In this case, the integration in eq 5 is two-dimensional in θ and ϕ. We calculate $W(\tau)$ by carrying out two-dimensional numerical integration of eq 5 for the general case of eq 6 given the values of the principal components of the dipole interaction tensor.

We automatically switch to one-dimensional integration for the case of axial symmetry.

In order to do the integration efficiently, a change of variable was made by setting $x = -\cos\theta$, where $\theta \in [0, \pi]$ and $x \in [-1, 1]$. Equation 5 is then transformed into eq 10

$$W(\tau) = \frac{1}{4\pi}\exp\left(-\frac{\tau}{T_1}\right)\int_0^{2\pi} d\phi\left[\int_{-1}^{1} dx\left\{\left[\cosh(R\tau) + \frac{\sinh(R\tau)}{2RT_1}\right]^2 + \frac{D^2}{4R^2}\sinh^2(R\tau)\right\}\right] \quad (10)$$

where D is related to x and ϕ by

$$D(r, x, \phi) = a(r)(1 - x^2)(\cos^2\phi - \sin^2\phi) + c(r)[x^2 - (1 - x^2)\sin^2\phi] \quad (11)$$

In the case of axial symmetry, eq 10 reduces to

$$W(\tau) = \frac{1}{2}\exp\left(-\frac{\tau}{T_1}\right)\int_{-1}^{1} dx\left\{\left[\cosh(R\tau) + \frac{\sinh(R\tau)}{2RT_1}\right]^2 + \frac{D^2}{4R^2}\sinh^2(R\tau)\right\} \quad (12)$$

where D is related to x by

$$D(r, x) = a(r)(1 - 3x^2) \quad (13)$$

The integrations in eqs 10 and 12 were carried out recursively with the extended trapezoidal rule for an integral over a function $f(x)$

$$I = \int_a^b f(x)\,dx \approx \left(\frac{f(x_0)}{2} + f(x_1) + \ldots + f(x_{n-1}) + \frac{f(x_n)}{2}\right)\left(\frac{b - a}{n}\right) \quad (14)$$

with Romberg integration, which uses polynomial extrapolation to speed up the integration.[89] For the integral in eq 12, convergence to 10^{-6} is usually accomplished within seven iterations with polynomial extrapolation, i.e., $n = 128$, using double-precision floating point numbers. For the integral in eq 10, the inner integral is usually converged to 10^{-7} within seven iterations, and the outer integral is usually converged to 10^{-5} within seven iterations. In the case when the value of R in eq 7 approaches zero, a power expansion over R was carried out including all terms up to $O(R^3)$ for $|R| \leq 10^{-10}$. This helps to avoid numerical instability in calculating the integrands in eqs 10 and 12. We calculated $W(\tau)$ from 0 to 2 μs with a step size of 0.5 μs (i.e., 500 points) to reproduce the initial ratio of fits in eq 4. The experimental values of the Ti^{3+} T_1 were used in the simulations (see Figure SM-4 and Table SM-4, Supporting Information).

The input parameters are the principal components of the $Car^{\bullet+}$−Ti^{3+} dipolar interaction, a and c, at a given value of the distance r obtained from the DFT calculations. The curve is calculated as a function of r and a best fit with the experimental curve determines r. The limits for the dipolar interaction were estimated using relationship between the dipolar coupling tensor H_{dd} and the second moment of the EPR line, $\langle H^2\rangle$:[90]

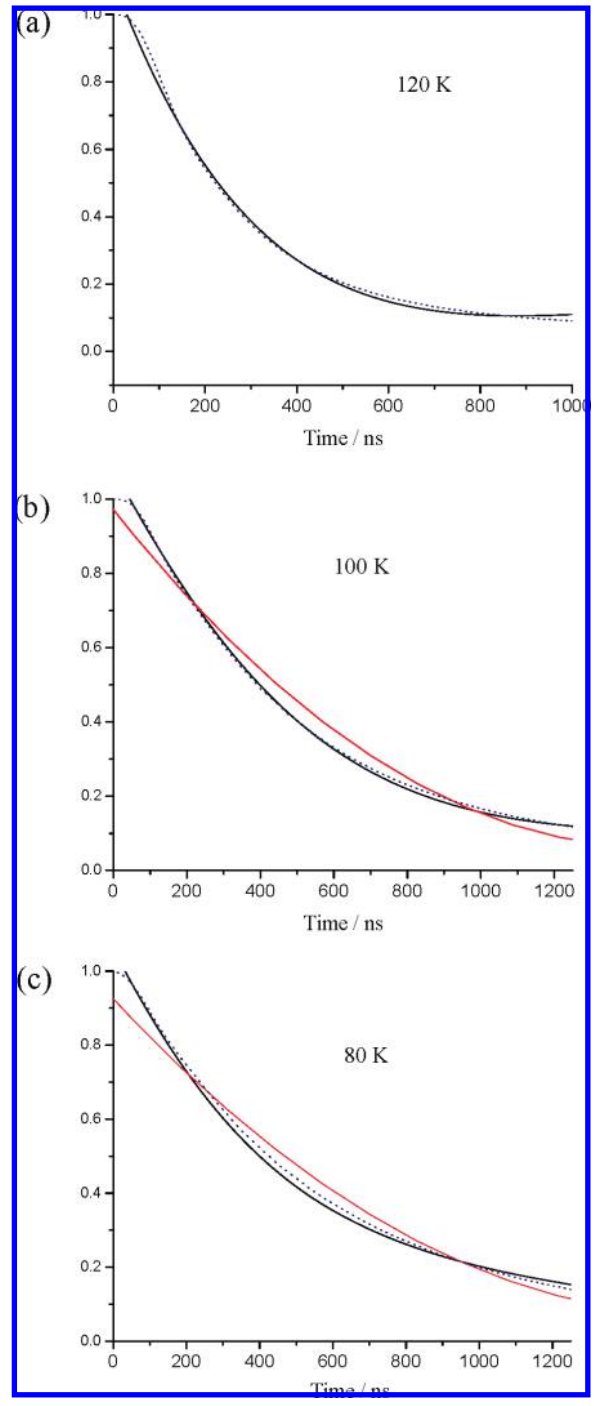

Figure 11. Experimental (solid black line) and calculated from eqs 10 and 12 (dotted blue line) ratios of the two-pulse echo decay fits in the presence and in the absence of Ti^{3+} for 7′-apo-7′-(4-carboxyphenyl)-β-carotene (**1**) using the dipolar components $a = 34.85$ MHz and $c = 42.5$ MHz at (a) 120 K, (b) 100 K, and (c) 80K. The time axis is the pulse spacing of the two-pulse echo. The curves (b) and (c) when simulated as exponentials (solid red line) did not show a good fit.

$$\langle H^2\rangle \sim {H_{dd}}^2/4 \quad (15)$$

$${H_{dd}}^2 = 1/3(a^2 + b^2 + c^2) \quad (16)$$

The continuous wave (CW) EPR spectra of $Car^{\bullet+}$ in MCM-41 and TiMCM-41 have a Gaussian line shape. For such a Gaussian EPR line, the second moment can be measured from the line-width broadening due to the presence of Ti^{3+}, which is proportional to the dipolar contribution:[90]

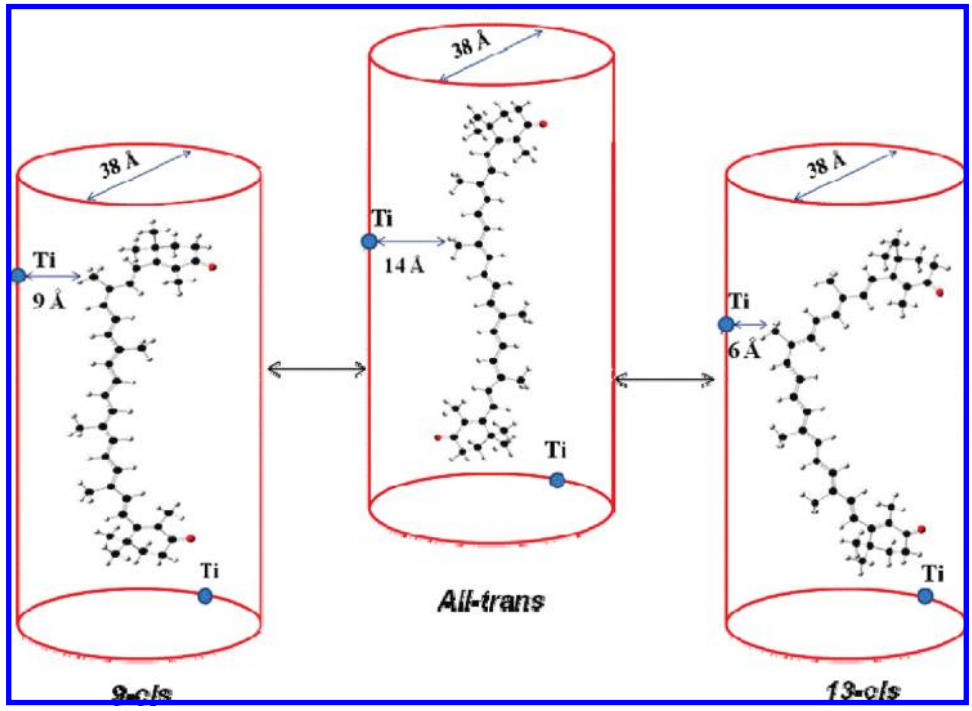

Figure 12. A schematic representation of canthaxanthin (**2**) oxidation in TiMCM-41 where the 9-*cis* and 13-*cis* isomers are formed from the *all-trans* carotenoid.

$$\langle H^2 \rangle = [(\Delta H_{pp}^{TiMCM})^2 - (\Delta H_{pp}^{MCM})^2]/4 \qquad (17)$$

As above, after subtraction of a slow component which contributes to the echo decay at times >600 ns, the experimental $W(\tau)$ was compared to the calculated ones from eqs 10 and 12 as shown in Figure 11. Fitting of the calculated curves from these equations to the experimental curves provides the interspin distance r. The best fit value for the interspin distance of $\mathbf{1}^{\bullet+}$/Ti^{3+} is 9.0 ± 2.0 Å, which is valid over a wide temperature range. The range of distances from 7 to 11 Å corresponds to an approximate range of $a \approx -c$ of 20 to 70 MHz (see Table 2). The distances obtained from these equations for canthaxanthin (**2**) and β-ionone, 10.0 ± 3.0 Å for canthaxanthin (**2**) and 10.0 ± 2.0 Å for β-ionone, are similar to those determined from the fit to the simpler $1/T_M - 1/T_{M0}$ expressions described above of 13.2 and 10.5 Å, respectively. We did not include J in our expression because, in the carotenoids, the unpaired spin is highly delocalized over the long carotenoid polyene chain. Fitting the experimental data with a simple exponential, which is a point dipole approximation including a large J value, shows a poor fit (Figure 11, b and c), which is consistent with our approach setting $J = 0$.

The variations in the interspin distances are likely to be due to the orientations of the different carotenoid isomers inside the pore. A schematic of the orientation of oxidized canthaxanthin in the TiMCM-41 mesopore is shown in Figure 12. The largest distance of 13−14 Å occurs when *all-trans* $Car^{\bullet+}$ with maximum spin density localized in the middle of the polyene chain interacts with the framework Ti^{3+} ion. The medium distance of 9 Å could be due to 9-*cis* $Car^{\bullet+}$, and the shortest distance of 6−7 Å is found when $Car^{\bullet+}$ is in its 13-*cis* conformation. The interspin distances determined with both methods are much smaller than the size of the carotenoid radicals (the length of the *all-trans* isomer is over 30 Å). Our definition for the interspin distance is the shortest distance between the Ti^{3+} ion and the radical as shown in Figure 12. As shown in Table 2, for the *all-trans* isomers of the carotenoid radicals, the calculated dipolar tensor components depend almost exclusively on the shortest distance between the Ti^{3+} ion and the radical.

The values of the interspin distances provide the information on the electron transfer and the possible location and orientation of the carotenoid in TiMCM-41 mesopore. The environment in a metal-substituted MCM-41 can cause an isomerization of the embedded Car via $Car^{\bullet+}$.[32] Photoisomerization of carotenoids has been confirmed by time-resolved resonance Raman spectroscopy, HPLC analysis[91] and 2D Raman correlation spectroscopy.[92] Our HPLC measurements confirmed the formation of 9- and 13-*cis*-$Car^{\bullet+}$ together with *all-trans*-$Car^{\bullet+}$ for canthaxanthin (**2**) in MCM-41 and TiMCM-41 with *cis*−*trans* ratios of ∼0.2−0.5.[32] Thus, *all-trans* radical cations can undergo subsequent isomerization producing *cis*-$Car^{\bullet+}$ isomers. In fact, the 9-*cis* and 13-*cis* isomers were calculated to be only 1.3 and 1.4 kcal/mol higher in energy, respectively, than the *all-trans* isomer for canthaxanthin (**2**), and 1.3 and 2.1 kcal/mol higher in energy, respectively, for its cation (Supporting Information). Our Mims ENDOR data (Supporting Information) in combination with the DFT calculations show the possibility of 9-*cis* and 13-*cis* $Car^{\bullet+}$ formation of **2** in TiMCM-41. As shown in Figure SM-1(A,B), *all-trans*-canthaxanthin (**2**) is difficult to fit across the pore. For the *cis* isomers such an orientation becomes possible as shown in Figure SM-1(C,D). However, the orientation with the canthaxanthin (**2**) vertically aligned along the pore is more likely for the *all-trans* and *cis* isomers due to lower steric constraints as shown in Figure 1C,D.

Conclusions

The present study demonstrates that pulsed EPR spectroscopy is a powerful tool to study the oxidation of carotenoids inside metal-substituted mesoporous materials. Pulsed ENDOR and 2D HYSCORE experiments revealed the nature of the carotenoid radicals produced in MCM-41 and TiMCM-41. An estimate of through space electron transfer distances from the carotenoid electron donor to the Ti(IV) electron acceptor site

in TiMCM-41 was obtained. To determine distances between the framework Ti(III) ion and the carotenoid radical, the effect of a rapidly relaxing metal spin on T_M of a slowly relaxing carotenoid spin was measured as a function of temperature in both MCM-41 and TiMCM-41. The significant increase in the relaxation rate, $1/T_M$, for β-ionone, 7′-apo-7′-(4-carboxyphenyl)-β-carotene, and canthaxanthin in TiMCM-41 is consistent with an interaction between the radical and the fast relaxing Ti^{3+} ion. The method of interspin distance determination involves the use of actual dipole−dipole interaction values and provides an improved approach for the data analysis. The method based on the point-dipole approximation usually used to determine interspin distances by relaxation measurements was modified to accommodate the fact that the distribution of unpaired spin density along the C22 polyene chain of the carotenoid is not a point dipole but that each carbon has approximately 0.05 excess alpha spin. The experimental and calculated $W(\tau)$ were fit by adjusting the components of the dipolar tensor. The proper values of the dipolar interaction, when the simulations match the experimental curves, were used for the distance determination. This method works well for the two cases of a monotonic relaxation rate increase and of a prominent peak at a certain temperature. The interspin distances between the carotenoid radical and the Ti^{3+} ion are 10.0 ± 3.0, 10.0 ± 2.0, and 9 ± 2.0 Å for canthaxanthin, β-ionone, and 7′-apo-7′-(4-carboxyphenyl)-β-carotene, respectively.

Acknowledgment. This work was supported by the Division of Chemical Sciences, Geosciences, Biosciences, Office of Basic Energy Sciences, Office of Science, the US Department of Energy, Grants DE-FG02-86ER13465 (L.D.K.), DE-FG02-03ER15481 (D.A.D., Catalysis Center program) and the National Science Foundation for EPR Instrument Grants CHE-0342921 and CHE-0079498. D.A.D. also thanks the Robert Ramsay Chair Fund of The University of Alabama for support. We thank Prof. Michael K. Bowman (The University of Alabama) for helpful discussions.

Supporting Information Available: Tables: Proton isotropic hyperfine couplings of isomers of the radicals and radical cations of (**1**) and (**2**) determined from pulsed ENDOR/HYSCORE analysis in MCM-41 and TiMCM-41 and DFT calculations including the assignments to the higher energy isomers for the neutral radicals; relaxation rates of canthaxanthin (**2**), carboxy-β-carotene (**1**), and β-ionone radicals in siliceous MCM-41 and in TiMCM-41; spin−lattice relaxation times of Ti^{3+} at various temperatures; relative energies of the isomers of the neutral radicals for (**1**) and (**2**); relative energies of the *trans* and *cis* isomers for the neutral and cation for (**2**); geometries and energies of the *trans* and *cis* isomers of canthaxanthin (**2**) and its cation. Figures: The structure of MCM-41 with *all-trans* (**2**), 9-*cis* (**2**), and 13-*cis* (**2**) inserted across the pore. Proton Mims ENDOR spectra of 7′-apo-7′-(4-carboxyphenyl)-β-carotene (**1**) at 20 K in MCM-41 and TiMCM-41 measured at different τ; proton Mims ENDOR spectra of canthaxanthin (**2**) in MCM-41 measured at different τ; inversion recovery with echo detection on logarithmic time scale for Ti(III) in (**1**)/TiMCM-41. This material is available free of charge via the Internet at http://pubs.acs.org.

References and Notes

(1) Beck, D. W. *Zeolite Molecular Sieves*; Wiley: New York, 1974.
(2) Beck, J. S.; Vartuli, J. C.; Roth, W. J.; Leonowicz, M. E.; Kresge, C. T.; Schmitt, K. D.; Chu, C. T-W.; Olson, D. H.; Sheppard, E. W.; McCullen, S. B.; Higgings, J. B.; Schlenker, J. L. *J. Am. Chem. Soc.* **1992**, *114*, 10834.
(3) Gratzel, M. *Heterogeneous Photochemical Electron Transfer*; CRC Press Inc.: Boca Raton, FL, 1988.
(4) Vansant, E. F.; Van Der Voort, P.; Vranchen, K. C. *Characterization and Chemical Modification of Silica Surfaces*; Elsevier: Amsterdam, 1995.
(5) Kevan, L. In *Photoinduced Electron Transfer. Part B*; Fox, M. A., Chanon, M., Eds.; Elsevier: Amsterdam, 1988; pp 329−384.
(6) Corma, A.; Fornes, V.; Garcia, H.; Miranda, M. A.; Sabater, A. *J. Am. Chem. Soc.* **1994**, *116*, 9767.
(7) Cano, M. L.; Cozens, F. L.; Garcia, H.; Marti, V.; Scaiano, J. C. *J. Phys. Chem.* **1996**, *100*, 18152.
(8) Sung-Suh, H. M.; Luan, Z.; Kevan, L. *J. Phys. Chem. B* **1997**, *101*, 10455.
(9) Faller, P.; Maly, T.; Rutherford, A. W.; MacMillan, F. *Biochemistry* **2001**, *40*, 320.
(10) Tracewell, C. A.; Vrettos, J. S.; Bautista, J. A.; Frank, H. A.; Brudvig, G. W. *Arch. Biochem. Biophys.* **2001**, *385*, 61.
(11) Lakshmi, K. V.; Poluektov, O. G.; Reifler, M. J.; Wagner, A. M.; Thurnauer, M. C.; Brudvig, G. W. *J. Am. Chem. Soc.* **2003**, *125*, 5005.
(12) Corma, A.; Navarro, M. T.; Perez-Pariente, J.; Sanchez, F. In *Studies in Surface Science and Catalysis, Vol. 84, Part I*; Weitkamp, J., Karge, H. G., Pfeifer, H., Holderich, W., Eds.; Elsevier: Amsterdam, 1994; pp 69−75.
(13) Luan, Z.; Cheng, C.-F.; Zhou, W.; Klinowski, J. *J. Phys. Chem.* **1995**, *99*, 1018.
(14) Zhao, D.; Goldfarb, D. *J. Chem. Soc., Chem. Commun.* **1995**, 875.
(15) Anpo, M.; Nakaya, H.; Kodama, S.; Kubokawa, Y. *J. Phys. Chem.* **1986**, *90*, 1633.
(16) Liu, Z.; Davis, R. J. *J. Phys. Chem.* **1994**, *98*, 1253.
(17) Topsoe, N.-Y. *Science* **1994**, *265*, 1217.
(18) Tuel, A.; Diab, J.; Gelin, P.; Dufaux, M.; Dutel, J.-F.; Ben Taarit, Y. *J. Mol. Catal.* **1991**, *68*, 45.
(19) Romano, U.; Esposito, A.; Maspero, F.; Neri, C.; Clerici, M. G. In *Studies in Surface Science and Catalysis*; Centi, G., Trifiro, F., Eds.; Elsevier: Amsterdam, 1990; Vol. 55, pp 33−41.
(20) Thomas, J. M.; Greaves, G. N. *Science* **1994**, *265*, 1675.
(21) Notari, B. *Adv. Catal.* **1996**, *41*, 253.
(22) Tuel, A.; Diab, J.; Gelin, P.; Dufaux, M.; Dutel, J.-F.; Tarit, Y. B. *J. Mol. Catal.* **1990**, *63*, 95.
(23) Ghorbel, A.; Tuel, A.; Jorda, E.; Ben Taarit, Y.; Naccache, C. In *Studies in Surface Science and Catalysis*; Bonneviot, L., Kaliaguine, S., Eds.; Elsevier: Amsterdam, 1995; Vol. 97, p 471.
(24) Prakash, A. M.; Sung-Suh, H. M.; Kevan, L. *J. Phys. Chem. B* **1998**, *102*, 857.
(25) Krishna, R. M.; Kurshev, V.; Kevan, L. *Phys. Chem. Chem. Phys.* **1999**, *1*, 2833.
(26) Krishna, R. M.; Prakash, A. M.; Kevan, L. *J. Phys. Chem. B* **2000**, *104*, 1796.
(27) Gao, Y.; Konovalova, T. A.; Xu, T.; Kispert, L. D. *J. Phys. Chem. B* **2002**, *106*, 10808.
(28) Micic, O. I.; Zhang, Y.; Cromach, K. R.; Trifunac, A. D.; Thurnauer, M. C. *J. Phys. Chem.* **1993**, *97*, 7277.
(29) Heimer, T. A.; Heilweil, E. J. *J. Phys. Chem. B* **1997**, *101*, 10990.
(30) Thurnauer, M. C.; Rajh, T.; Tiede, D. M. *Acta Chem. Scand.* **1997**, *51*, 610.
(31) Gao, Y.; Konovalova, T. A.; Lawrence, J. N.; Smitha, M. A.; Nunley, J.; Schad, R.; Kispert, L. D. *J. Phys. Chem. B* **2003**, *107*, 2459.
(32) Gao, Y.; Kispert, L. D.; Konovalova, T. A.; Lawrence, J. *J. Phys. Chem. B* **2004**, *108*, 9456.
(33) Kispert, L. D.; Bowman, M. K.; Norris, J. R.; Brown, M. S. *J. Chem. Phys.* **1982**, *76*, 26.
(34) Maschmeyer, T.; Rey, F.; Sankar, G.; Thomas, G. M.; Sankar, G.; Thomas, G. M. *Nature* **1995**, *378*, 159.
(35) Konovalova, T. A.; Gao, Y.; Schad, R.; Kispert, L. D.; Saylor, C. A.; Brunel, L. C. *J. Phys. Chem. B* **2001**, *105*, 7459.
(36) Grupp, A.; Mehring, M. In *Modern Pulsed and Continuous-wave Electron Spin Resonance*; Kevan, L., Bowman, M. K., Eds.; Wiley: New York, 1990; pp 195−229.
(37) Astashkin, A. SimBud−EPR simulation program, University of Arizona, http://quiz2.chem.arizona.edu/epr/epr_000006.htm.
(38) *Gaussian 03, Revision E.01*; Frisch, M. J.; Trucks, G. W.; Schlegel, H. B.; Scuseria, G. E.; Robb, M. A.; Cheeseman, J. R.; Montgomery, J. A., Jr.; Vreven T.; Kudin, K. N.; Burant, J. C.; Millam, J. M.; Iyengar, S. S.; Tomasi, J.; Barone, V.; Mennucci, B.; Cossi, M.; Scalmani, G.; Rega, N.; Petersson, G. A.; Nakatsuji, H.; Hada, M.; Ehara, M.; Toyota, K.; Fukuda, R.; Hasegawa, J.; Ishida, M.; Nakajima, T.; Honda, Y.; Kitao, O.; Nakai, H.; Klene, M.; Li, X.; Knox, J. E.; Hratchian, H. P.; Cross, J. B.; Adamo, C.; Jaramillo, J.; Gomperts, R.; Stratmann, R. E.; Yazyev, O.; Austin, A. J.; Cammi, R.; Pomelli, C.; Ochterski, J. W.; Ayala, P. Y.; Morokuma, K.; Voth, G. A.; Salvador, P.; Dannenberg, J. J.; Zakrzewski, V. G.; Dapprich, S.; Daniels, A. D.; Strain, M. C.; Farkas, O.; Malick, D. K.; Rabuck, A. D.; Raghavachari, K.; Foresman, J. B.; Ortiz, J. V.; Cui, Q.; Baboul, A. G.; Clifford, S.; Cioslowski, J.; Stefanov, B. B.; Liu, G.; Liashenko, A.; Piskorz, P.; Komaromi, I.; Martin, R. L.; Fox, D. J.; Keith, T.; Al-Laham, M. A.;

Peng, C. Y.; Nanayakkara, A.; Challacombe, M.; Gill, P. M. W.; Johnson, B.; Chen, W.; Wong, M. W.; Gonzalez, C.; Pople, J. A. Gaussian, Inc.: Pittsburgh PA, 2003.

(39) (a) Becke, A. D. *J. Chem. Phys.* **1993**, *98*, 5648. (b) Lee, C.; Yang, W.; Parr, R. G. *Phys. Rev. B* **1988**, *37*, 785.

(40) Hehre, W. J.; Radom, L.; Schleyer, P. R.; Pople, J. A. *Ab Initio Molecular Orbital Theory*; John Wiley and Sons: New York, 1986.

(41) Gao, Y.; Focsan, A. L.; Kispert, L. D.; Dixon, D. A. *J. Phys. Chem. B* **2006**, *110*, 24750.

(42) Schafer, A.; Horn, H.; Ahlrichs, R. *J. Chem. Phys.* **1992**, *97*, 2571.

(43) Cho, H.; Felmy, A. R.; Craciun, R.; Keenum, J. P.; Shah, N.; Dixon, D. A. *J. Am. Chem. Soc.* **2006**, *128*, 2324.

(44) *AMPAC 8, 1992−2004*; Semichem, Inc., PO Box 1649, Shawnee, KS 66222.

(45) (a) Chelikowsky, J. R.; Troullier, N.; Martins, J. L.; King, H. E., Jr. *Phys. Rev. B* **1991**, *44*, 489. (b) Hazen, R. M.; Finger, L. W.; Hemley, R. J.; Mao, H. K. *Solid State Commun.* **1989**, *72*, 507. (c) Levien, L.; Prewitt, C. T.; Weidner, D. J. *Am. Mineral.* **1980**, *65*, 920.

(46) Kleestorfer, K.; Vinek, H.; Jentys, A. *J. Mol. Catal. A* **2001**, *166*, 53.

(47) Jeevarajan, A. S.; Khaled, M.; Kispert, L. D. *J. Phys. Chem.* **1994**, *98*, 7777.

(48) Jeevarajan, A. S.; Kispert, L. D.; Avdievich, N. I.; Forbes, M. D. E. *J. Phys. Chem.* **1996**, *100*, 669.

(49) Kurreck, H.; Bock, M.; Bretz, N.; Elsner, M.; Kraus, H.; Lubitz, W.; Mobius, K. *J. Am. Chem. Soc.* **1984**, *106*, 737.

(50) Dikanov, S. A.; Bowman, M. K. *J. Magn. Reson. A* **1995**, *116*, 125.

(51) Astrakas, L.; Deligiannakis, Y.; Mitrikas, G.; Kordas, G. *J. Chem. Phys.* **1998**, *109*, 8612.

(52) Dikanov, S. A.; Tyryshkin, A. M.; Bowman, M. K. *J. Magn. Reson. A* **2000**, *144*, 228.

(53) Dikanov, S. A.; Bowman, M. K. *J. Biol. Inorg. Chem.* **1998**, *3*, 18.

(54) Piekara-Sady, L.; Khaled, M. M.; Bradford, E.; Kispert, L. D.; Plato, M. *Chem. Phys. Lett.* **1991**, *186*, 143.

(55) Wu, Y.; Piekara-Sady, L.; Kispert, L. D. *Chem. Phys. Lett.* **1991**, *180*, 573.

(56) Piekara-Sady, L.; Jeevarajan, S. A.; Kispert, L. D. *Chem. Phys. Lett.* **1993**, *207*, 173.

(57) Jeevarajan, A. S.; Kispert, L. D.; Piekara-Sady, L. *Chem. Phys. Lett.* **1993**, *209*, 269.

(58) Focsan, A. L.; Bowman, M. K.; Konovalova, T. A.; Molnár, P.; Deli, J.; Dixon, D. A.; Kispert, L. D. *J. Phys. Chem. B* **2008**, *112*, 1806.

(59) Poole, C. P.; Farach, H. *Relaxation in Magnetic Resonance*; Academic Press: New York, 1971; pp. 196−200.

(60) Kulikov, A. V.; Likhtenshtein, G. I. *Adv. Mol. Relax. Interact. Proc.* **1977**, *10*, 47.

(61) Bowman, M. K.; Norris, J. R. *J. Phys. Chem.* **1982**, *86*, 3385.

(62) Kar, L.; Johnson, M. E.; Bowman, M. K. *J. Magn. Reson.* **1987**, *75*, 397.

(63) Zhou, Y.; Bowler, B. E.; Lynch, K.; Eaton, S. S.; Eaton, G. R. *Biophys. J.* **2000**, *79*, 1039.

(64) Norris, J. R.; Thurnauer, M. C.; Bowman, M. K. *Adv. Biol. Med. Phys.* **1980**, *17*, 365.

(65) Calvo, R.; Isaacson, R. A.; Abresh, E. C.; Okamura, M. Y.; Feher, G. *Biophys. J.* **1982**, *37*, 111.

(66) Styring, S. A.; Rutherford, A. W. *Biochemistry* **1988**, *27*, 4915.

(67) Innes, J. B.; Brudvig, G. W. *Biochemistry* **1989**, *28*, 1116.

(68) Hirsh, D. J.; Beck, W. F.; Innes, J. B.; Brudvig, G. W. *Biochemistry* **1992**, *31*, 532.

(69) Lakshmi, K. V.; Brudvig, G. W. In *Biological magnetic resonance*; Berliner, L. J., Eaton, S. S., Eaton, G. R., Eds.; Kluwer Academic/Plenum: New York, 2000; Vol. 19, pp 513−567.

(70) Lakshmi, K. V.; Brudvig, G. W. *Curr. Opin. Struct. Biol.* **2001**, *11*, 523.

(71) Deligiannakis, Y.; Rutherford, A. W. *Biochemistry* **1996**, *35*, 11239.

(72) Bittl, R.; Kawamori, A. In *Advances in Photosynthesis and Respiration*; Wyndrzynski, T. J., Satoh, K., Eds.; Springer: Dordrecht, The Netherlands, 2005; Vol. 22, pp 389−402.

(73) Zhou, Y.; Bowler, B. E.; Eaton, G. R.; Eaton, S. S. *J. Magn. Reson.* **1999**, *139*, 165.

(74) Budker, V.; Du, J.-L.; Seiter, M.; Eaton, G. R.; Eaton, S. S. *Biophys. J.* **1995**, *68*, 2531.

(75) Rakowsky, M. H.; More, K. M.; Kulikov, A. V.; Eaton, G. R.; Eaton, S. S. *J. Am. Chem. Soc.* **1995**, *117*, 2049.

(76) Seiter, M. V.; Budker, J.-L.; Du, G. R.; Eaton, G. R.; Eaton, S. S. *Inorg. Chim. Acta* **1998**, *273*, 354.

(77) Eaton, S. S.; Eaton, G. R. In *Biological Magnetic Resonance*; Berliner, L. J., Eaton, S. S., Eaton, G. R., Eds.; Kluwer Academic Press: New York, 2000; Vol. 19, pp 347−381.

(78) Slichter, C. P. *Principles of Magnetic Resonance*; Springer: Berlin, 1990.

(79) Hilczer, W.; Goslar, J.; Gramza, M.; Hoffmann, S. K.; Blicharski, W.; Osyczka, A.; Turyna, B.; Froncisz, W. *Chem. Phys. Lett.* **1995**, *247*, 601.

(80) Zhidomirov, G. M.; Salikhov, K. M. *Sov. Phys. JETP* **1969**, *29*, 1037.

(81) Salikhov, K. M.; Semenov, A. G.; Tsvetkov, Yu. D. *Electron Spin Echo and Its Applications*; Nauka: Novosibirsk, Russia, 1976.

(82) Stillman, A. E.; Schwartz, L. J.; Freed, J. H. *J. Chem. Phys.* **1980**, *73*, 3502.

(83) Salikhov, K. M.; Dzuba, S. A.; Raitsimring, A. M. *J. Magn. Reson.* **1981**, *42*, 255.

(84) Dzuba, S. A.; Salikhov, K. M.; Tsvetkov, Yu. D. *Chem. Phys. Lett.* **1981**, *79*, 568.

(85) Bowman, M. K.; Kevan L. *Time Domain Electron Spin Resonance*; Kevan, L., Schwartz, R. N., Eds.; Wiley: New York, 1979; pp 68−105.

(86) Salikhov, K. M.; Tsvetkov, Y. D. In *Time Domain Electron Spin resonance*, Kevan, L., Schwartz, R. N., Eds.; Wiley: New York, 1979; pp 231−277.

(87) Rao, S. B. K.; Tyryshkin, A. M.; Roberts, A. G.; Bowman, M. K.; Kramer, D. M. *Biochemistry* **2000**, *39*, 3285.

(88) Lide, D. R., Ed.; *CRC Handbook of Chemistry and Physics*, 88th ed.; CRC Press/Taylor and Francis: Boca Raton, FL (Internet Version 2008) (http://www.hbcpnetbase.com).

(89) (a) Press, W. H.; Flannery, B. P.; Teukolsky, S. A.; Vetterling, W. T. *Numerical Recipes in FORTRAN 77: The Art of Scientific Computing*, 2nd ed.; Cambridge University Press: Cambridge, UK, 1992. (b) Press, W. H.; Teukolsky, S. A.; Vetterling, W. T.; Flannery, B. P. *Numerical Recipes in FORTRAN 90: The Art of Scientific Computing*, 2nd ed.; Cambridge University Press: Cambridge, UK, 1996.

(90) Bales, B. L.; Bowman, M. K.; Kevan, L.; Schwartz, R. N. *J. Chem. Phys.* **1975**, *63*, 3008.

(91) Hashimoto, H.; Koyama, Y. *J. Phys. Chem.* **1988**, *92*, 2101.

(92) Noda, I.; Marcott, C. *J. Phys. Chem. A* **2002**, *106*, 3371.

(93) Focsan, A. L. Ph.D. Thesis, The University of Alabama, May 2008.

JP811369H